International Journal of Heat and Technology
Vol. 40, No. 1, February, 2022, pp. 193-200
Journal homepage: http://iieta.org/journals/ijht

# Bonding Performance and Thermomechanical Coupling Analysis of Iron Ore Tailings Reinforced Concrete

Yuhan Bai, Jianheng Sun*, Ruolan Zhang

Department of Civil Engineering, Hebei Agricultural University, Baoding 071000, China

Corresponding Author Email: sjh@hebau.edu.cn

https://doi.org/10.18280/ijht.400123

**Received:** 29 September 2021
**Accepted:** 15 December 2021

***Keywords:***
*reinforced concrete, bonding performance, thermal stress, thermal strain*

**ABSTRACT**

After long-term use at high temperatures, the iron ore tailings (IOT) reinforced concrete will suffer from problems like carbonization, corrosion, and durability decline. It is highly practical to analyze the bonding performance and thermomechanical coupling mechanism of IOT reinforced concrete. The relevant literature rarely considers the influence of temperature over the bonding performance of samples, or prepares samples from IOT concrete. There are very limited results on the similarity of the temperature field and mechanical response of reinforced concrete under high temperatures. To solve the problem, this paper constructs a bond slip curve model for the IOT-reinforced concrete interface, and provides a way to plot the mean bond slip curve, before computing the bond stress distribution, as well as local bond stress-relative slip distribution. Next, the authors summarized the thermal parameters of the IOT concrete material, and the high-temperature relationship between thermal stress and thermal strain. Finally, sixteen central pull-out tests were carried out on central pull-out samples by applying strain gages into rebar slots. In this way, the authors obtained the results on the bonding performance and thermomechanical coupling analysis of IOT reinforced concrete.

## 1. INTRODUCTION

The rapid urbanization in China leads to a rising demand for reinforced concrete [1-6]. To fulfil the demand, a huge sum of sand and gravels has been mined, causing serious damages to rivers and mountains. The environmental degradation is accompanied by the growing shortage of construction sand [7-10]. Facing the lack of resources, and enhanced awareness of environmental protection, it is a national strategy to prepare building materials from ore tailings. For example, the preparation of iron ore tailings (IOT) concrete can effectively alleviate the contradiction between resources and the environment [11-16]. After long-term use at high temperatures, the IOT reinforced concrete will suffer from problems like carbonization, corrosion, and durability decline, and even engineering safety risks. It is highly practical to analyze the bonding performance and thermomechanical coupling mechanism of IOT reinforced concrete.

The macroscopic synthetic fiber reinforced IOT concrete is an environmentally friendly building material. The fibers are mixed into the recycled IOT to improve the performance of IOT concrete. Zhao et al. [17] systematically studied the mechanical performance of the macroscopic synthetic fiber reinforced IOT concrete. After selecting the macroscopic synthetic fibers of two different IOT substitution rates and six volume fractions (with an interval of 1.0%), Zhao explored the influence of IOT, aspect ratio, elastic modulus, and tensile strength of the macroscopic synthetic fiber over the mechanical performance of the concrete. The IOT, which has caused a severe eco-environmental problem, has been gradually adopted as a construction material. However, the high-volume density of the IOT as an aggregate hinders the concrete performance. Gu et al. [18] investigated the influence of hydroxypropyl methylcellulose (HPMC) over the workability, mechanical performance, and durability of the concrete prepared from the recycled IOT aggregate. The mercury intrusion method (MIC) and scanning electron microscopy (SEM) were adopted to examine the mechanism of the HPMC acting on the workability and mechanical performance of IOT concrete.

The key to preventing building fires is to design and develop fireproof buildings. To assess the high-temperature performance of common concrete (CC) and ultra-high-performance fiber reinforced concrete (UHPFRC), Ashkezari et al. [19] explored the coefficient of thermal expansion, weight loss, and residual compressive strength, and adopted two different curing methods (non-heating, and heating), and steel microfiber inclusions of two different mix ratios. On this basis, Ashkezari evaluated the mechanical performance of CC and UHPFRC, including compressive strength, splitting strength, bending strength, and elastic modulus. Makeeva et al. [20] specifically studied the stress state of large concrete structure and reinforced concrete structure under the temperature of the construction period, and analyzed the thermal stress state of large volume concrete floor slabs with a thickness of 1m. Without considering the temperature effect, their approach successfully evaluates the thermal stress state of numerous slabs in building foundations, and ensures that the thermal stress of the structure will not deviate significantly from the actual graph of tensile deformation.

Some domestic and foreign scholars have tested and theorized the bonding performance of reinforced concrete, analyzed the crack forms of samples, and constructed the piecewise constitutive equation of the bond slip curve.

However, the relevant literature rarely considers the influence of temperature over the bonding performance of samples, or prepares samples from IOT concrete. There are very limited results on the similarity of the temperature field and mechanical response of reinforced concrete under high temperatures.

Therefore, this paper explores the bonding performance and thermomechanical coupling mechanism of IOT reinforced concrete. The main contents are as follows: (1) The authors constructed a bond slip curve model for the IOT-reinforced concrete interface, provided a way to plot the mean bond slip curve, and computed the bond stress distribution, as well as local bond stress-relative slip distribution. (2) The authors summarized the thermal parameters of the IOT concrete material, and the high-temperature relationship between thermal stress and thermal strain. (3) The authors conducted sixteen central pull-out tests were carried out on central pull-out samples by applying strain gages into rebar slots, and obtained the results on the bonding performance and thermomechanical coupling analysis of IOT reinforced concrete.

## 2. BONDING PERFORMANCE ANALYSIS

The first task of this paper is to build an improved bond slip model for the IOT reinforced concrete. Here, the bond slip curve is divided into four segments: the elastic microslip segment, the rising segment, the declining segment, and the residual segment. The Weibull model equation was employed to fit the elastic microslip segment. Let $(p\text{-}p_t)/(p_v\text{-}p_t)$ be the explanatory variable; $r\text{-}r_t)/(r_v\text{-}r_t)$ be the explanatory variable. Then, we have:

$$b = \phi_1 - \phi_2 t^{-\phi_3 a^{\phi_4}} \tag{1}$$

Let $p_v$ and $r_v(r_{v1},r_{v2})$ be the bonding stress and slip amount at the peak slip points $X_v$, and $X_{v1}$ in the bond slip curve, respectively; $p_s$ and $R_s$ be the bonding stress and slip amount of the residual slip point $X_s$, respectively; $p_t$, and $r_t$ be the bonding stress and slip amount of the elastic slip point $X_t$, respectively; $\varphi_1$, $\varphi_2$, $\varphi_3$, and $\varphi_4$ be the parameters fitted from test data. If the slip bond model of the IOT reinforced concrete does not contain an obvious horizontal segment, then the micro-slip segment can be expressed as:

$$p = \frac{p_t}{r_t} \times r, 0 < r < r_t \tag{2}$$

The rising segment and declining segment can be respectively expressed as:

$$p = (p_v - p_t) \times \left( \phi_1 - \phi_2 t^{-\phi_3 \left( \frac{r - r_t}{r_v - r_t} \right)^{\phi_4}} \right) + p_t, r_t < r < r_v \tag{3}$$

$$p = p_v - \left( \frac{p_v - p_s}{r_v - r_s} \right) \times (r_v - r), r_v < r < r_s \tag{4}$$

The residual segment can be expressed as:

$$p = p_s, r > r_s \tag{5}$$

If the slip bond model contains an obvious horizontal segment, then the micro-slip segment can be expressed as:

$$p = \frac{p_t}{r_t} \times r, 0 < r < r_t \tag{6}$$

The rising segment can be expressed as:

$$p = (p_v - p_t) \times \left( \phi_1 - \phi_2 t^{-\phi_3 \left( \frac{r - r_t}{r_{v1} - r_t} \right)^{\phi_4}} \right) + p_t, r_t < r < r_{v1} \tag{7}$$

The horizontal segment can be expressed as:

$$p = p_v, r_{v1} < r < r_{v2} \tag{8}$$

The declining segment and the residual segment can be respectively expressed as:

$$p = p_v - \left( \frac{p_v - p_s}{r_{v2} - r_s} \right) \times (r_{v2} - r), r_{v2} < r < r_s \tag{9}$$

$$p = p_s, r > r_s \tag{10}$$

To obtain the mean bond slip curve of the IOT reinforced concrete, the mean bonding strength and mean slip of each sample can be derived from the load and free end slip measured in tests. It is assumed that the bonding strength between rebar and concrete is uniformly distributed along the anchor length. Let d be the rebar diameter; l be the bonding length; $\Psi$ be the additional load. Then, we have:

$$\overline{p} = \frac{\Psi}{\pi d l} \tag{11}$$

The next step is to compute the bonding stress distribution. For a microsegment of rebar, the bonding stress of the rebar in the elastic phase is generally calculated through the strain measured from the microsegment in the equilibrium state. Let $A_n$ be the cross-sectional area; $E_S$ be the elastic modulus of the rebar; $\Delta\varepsilon$ be the stress difference between adjacent measuring points of the rebar; $C_e$ be the effective circumference of the rebar area in contact with concrete; $\Delta l$ be the interval between strain gages. Then, we have:

$$p = \frac{A_n E_S \Delta\varepsilon}{C_e} \tag{12}$$

The bonding stress calculated from each load level is accumulated along the free end to the load end. In theory, the cumulative value should be equal to the tensions $\Gamma_i$ and $\Gamma_i$ at the load end:

$$\Gamma_i = \sum_{i=1}^{n} p_i \cdot C_e \cdot \Delta l \tag{13}$$

If the two sides of formula (13) are not equal, the microsegment can be finetuned according to their difference.

Furthermore, it is necessary to compute the local bonding stress – relative slip distribution. In the anchor length, the relative slip is determined by the unique difference between

the various steel bars and concrete. Let $A_c$ and $A_s$ be the cross-sectional areas of the concrete and rebar, respectively; $\sigma_{ci}^*$ be the mean stress on the cross-sectional area of the concrete at the i-th measuring point; $\sigma_{si}$ be the rebar stress at the i-th measuring point. The following can be deduced from the measured rebar strain and microsegment equilibrium equation:

$$\sigma_{ci}^* A_c + \sigma_{si} A_s = 0 \tag{14}$$

Let $S_f$ be the displacement at the free end of the rebar; $\varepsilon_{si}$, and $\varepsilon_{ci}$ be the strains of rebar and concrete at each measuring point, respectively; $\Delta l_{si}$, and $\Delta l_{ci}$ be the deformations of rebar and concrete along the length of each microsegment, respectively. The slip of the concrete can be obtained by integrating the relative slips of microsegments along the anchor length. In the anchor length, the relative slip between rebar and concrete can be calculated by:

$$S_x = S_f + \sum_i^k = \Delta l_{si} + \Delta l_{ci} \tag{15}$$

where,

$$\begin{cases} \Delta l_{si} = \dfrac{\varepsilon_{si} + \varepsilon_{s(i+1)}}{2} l_i \\ \Delta l_{ci} = \dfrac{\varepsilon_{ci} + \varepsilon_{c(i+1)}}{2} l_i \end{cases} \tag{16}$$

## 3. THERMOMECHANICAL COUPLING ANALYSIS

Under high temperatures, the column sections of reinforced concrete can form a transient temperature field. In this case, the mechanical performance of the IOT reinforced concrete is affected by temperature. To disclose the similarity of the temperature field and mechanical response of reinforced concrete under high temperatures, this paper carries out finite-element simulation of the thermomechanical response of reinforced concrete, and compares the reinforced concretes with different mix ratios through sequential thermomechanical coupling.

Let $\sigma_{BE}$ and $\tau_{BE}$ be the density and specific heat capacity of the IOT concrete, respectively. The volumetric heat capacity of the IOT concrete is the product between $\sigma_{BE}$ and $\tau_{BE}$. Then, we have:

$$\begin{cases} \sigma_{BE}\tau_{BE} = (0.005\delta + 1.65)\times 10^6, \\ 0\,^oC \le \delta \le 180\,^oC \\ \sigma_{BE}\tau_{BE} = 2.68\times 10^6, \\ 180\,^oC < \delta \le 380\,^oC \\ \sigma_{BE}\tau_{BE} = (0.014\delta - 2.55)\times 10^6, \\ 380\,^oC < \delta \le 480\,^oC \\ \sigma_{BE}\tau_{BE} = (-0.014\delta + 9.8)\times 10^6, \\ 480\,^oC < \delta \le 580\,^oC \\ \sigma_{BE}\tau_{BE} = 2.44\times 10^6, \\ \delta > 580\,^oC \end{cases} \tag{17}$$

The peak specific heat capacity $\tau_{max}$ corresponds to the temperature range of 100℃~200℃. Let $\eta_{SU}$ be the mass water content of the IOT concrete. Then, the peak specific heat capacity $\tau_{max}$ at different water contents can be calculated by:

$$\begin{cases} \tau_{max} = 1885, \\ \eta_{SU} < 1.88\% \\ \tau_{max} = 1885 + (2800 - 1885)(\eta_{SU} - 1.88\%)(3.7\% - 2\%), \\ 1.88\% \le \eta_{SU} < 3.7\% \\ \tau_{max} = 2750 + (5560 - 2800)(\eta_{SU} - 3.7\%)(9.7\% - 3.7\%), \\ 3.7\% \le \eta_{SU} < 9.7\% \\ \tau_{max} = 5560, \\ \eta_{SU} \ge 9.7\% \end{cases} \tag{18}$$

Then, the thermal conductivity coefficient of the IOT concrete can be calculated by:

$$\begin{cases} \mu_p = -0.0009\delta + 2, 0\,^oC \le \delta \le 750\,^oC \\ \mu_p = 1.15, \delta > 750\,^oC \end{cases} \tag{19}$$

The thermal expansion coefficient of the IOT concrete can be calculated by:

$$\beta_{BE} = (0.0079\delta + 5.5)\times 10^{-6} \tag{20}$$

The volumetric heat capacity $\sigma_{RE}\tau_{RE}$ of the rebar can be calculated by:

$$\begin{cases} \sigma_{RE}\tau_{RE} = (0.0035\delta + 3.22)\times 10^6, \\ 0\,^oC \le \delta \le 680\,^oC \\ \sigma_{RE}\tau_{RE} = (0.066\delta - 35.5)\times 10^6, \\ 680\,^oC < \delta \le 780\,^oC \\ \sigma_{RE}\tau_{RE} = (-0.079\delta + 69.84)\times 10^6, \\ 780\,^oC < \delta \le 880\,^oC \\ \sigma_{RE}\tau_{RE} = 5.01\times 10^6, \\ \delta > 880\,^oC \end{cases} \tag{21}$$

The rebar density does not change significantly under high temperatures. Thus, the thermal conductivity coefficient $\mu_{RE}$ of the rebar can be calculated by:

$$\begin{cases} \mu_{RE} = -0.019\delta + 55, 0\,^oC \le \mu_{RE} \le 880\,^oC \\ \mu_{RE} = 30.2, \mu_{RE} > 880\,^oC \end{cases} \tag{22}$$

The thermal expansion coefficient $\beta_{RE}$ of the rebar can be calculated by:

$$\beta_{RE} = \begin{cases} (0.0035\delta + 13.2)\times 10^{-6}, \delta < 880\,^oC \\ 15.4\times 10^{-6}, \delta \ge 880\,^oC \end{cases} \tag{23}$$

Let $g_{BE}$ and $\rho_{BE}$ be the thermal stress and thermal strain of the IOT concrete, respectively; $g'_{BE}$ be the axial compressive strength of the IOT concrete under high temperatures; $\rho_{max}$ be the strain corresponding to the peak thermal stress of the IOT concrete; $g'_{BE0}$ be the axial compressive strength of the IOT concrete at normal temperature. Then, the thermal stress-

thermal strain relationship of the IOT concrete at high temperatures can be expressed as:

$$\begin{cases} g_{BE} = g'_{BE}\left[1-\left(\dfrac{\rho_{max}-\rho_{BE}}{\rho_{max}}\right)^2\right], \rho_{BE} \le \rho_{max} \\ g_{BE} = g'_{BE}\left[1-\left(\dfrac{\rho_{BE}-\rho_{max}}{3\rho_{max}}\right)^2\right], \rho_{BE} > \rho_{max} \end{cases} \tag{24}$$

$$\begin{cases} g'_{BE} = g'_{BE0}, \delta < 450^{\circ}C \\ g'_{BE} = g'_{BE0}\left[2.011-2.353\dfrac{\delta-20}{1000}\right], \delta \ge 450^{\circ}C \end{cases} \tag{25}$$

$$\rho_{max} = 0.0025+\left(6\delta+0.04\delta^2\right)\times 10^6 \tag{26}$$

When it comes to the thermal stress-thermal strain relationship of the rebar at high temperatures, it is assumed that the rebar elastic modulus in tensile state equals that in compressive state, before the rebar reaches the peak thermal strain $\rho_{Bel}$. Then, the peak tensile thermal stress $g'_{KL}$ and peak compressive thermal stress $g'_{BE}$ of the rebar satisfy:

$$g'_{KL} = 0.0889 g'_{BE} \tag{27}$$

Under high temperatures, the thermal stress drops linearly, after the rebar reaches the peak strain $\rho_{Bel}$. When the thermal strain of the rebar reaches $2\rho_{Bel}$, the corresponding stress of the rebar stands at $0.889g'_{KL}$, and will remain so thereafter.

When the rebar's thermal strain $\rho_{CO}$ is below the peak thermal strain $\rho_C$, the linear relationship between the thermal stress and thermal strain of the rebar has a constant slope. Hence, the elastic modulus of the rebar at high temperatures is the secant modulus at $\rho_{CV}$. If $\rho_{CO}$ is far greater than $\rho_{CV}$, the thermal stress of the rebar is linearly correlated with the thermal strain of the rebar. Let $g_b$ be the thermal stress of the rebar; $g_{b0}$ be the yield strength of the rebar at normal temperature. The relationship between $g_b$ and $g_{b0}$ can be expressed as:

$$\begin{cases} g_b = \dfrac{g(\delta,0.001)}{0.001}\rho_{CO}, \rho_{CO} \le \rho_{CV} \\ g_b = \dfrac{g(\delta,0.001)}{0.001}\rho_{CV} \\ \quad + g\left(\delta,\left(\rho_{CO}-\rho_{CV}+0.001\right)\right)-g(\delta,0.001), \\ \qquad \rho_{CO} > \rho_{CV} \end{cases} \tag{28}$$

$$\rho_{CV} = 4\times 10^6 g_{b0} \tag{29}$$

$$\begin{aligned} g(\delta,0.001) &= (50-0.04\delta) \\ &\times\left\{1-exp\left[(-30+0.03\delta)\sqrt{0.001}\right]\right\}\times 6.9 \end{aligned} \tag{30}$$

## 4. EXPERIMENTS AND RESULTS ANALYSIS

Our experiments use the following materials: The cement is the P.O 42.5R ordinary Portland cement (Hubei Jinglan Cement Group Co., Ltd., China). Grade 2 fly ash, IOT powder, IOT sands, and IOT stones were all obtained from Qian'an, northern China's Hebei Province. The IOT powder was ground to the specific surface area of 538.9 $m^2$/kg. The mortar specimens were prepared and cured for 28 days. Then, the activity index was measured as 66.8%. The rebars are HRB400 deformed bars with a diameter of 18mm or 25mm. Four types of concrete were designed for the experiments: 1. Fly ash concrete; 2. IOT powder concrete; 3. IOT power-IOT sand concrete; 4. IOT concrete. The rebar diameter was set to 18mm and 25mm. The concrete strength was set to C35 and C40. Hence, a total of 48 samples were prepared for 16 groups. Each group contains 3 samples.

The central pull-out sample is illustrated in Figure 1, where 1 is the rebar extruding from the free end; 2 is the position for applying strain gages in the rebar slot; 3 is the non-bonded area formed by the polyvinyl chloride (PVC) casing; 4 is the concrete block; 5 is the rebar.

Figure 2 explains how to open a slot in the rebar and apply the strain gages. In the bonded area, a shallow slot is opened horizontally along the rebar surface. Then, the foil strain gages are placed in the slot. After waterproofing treatment, the slot is sealed with epoxy resin. The wires of the gages are led to the concrete surface via fine soft plastic tubes. The gage interval is denoted by $\Delta l$. Table 1 summarizes the compressive and splitting strengths of the concrete blocks.

As shown in Figure 3, the samples were damaged in two forms: the pull-out damage of rebar, and the splitting damage of concrete. (1) The pull-out damage of rebar is a form of ductile failure. After the load reaches the limit, the slip between the rebar and the concrete is far greater than that in the load rising segment. As a result, the rebar and concrete suffer from shear damages, and the rebar is pulled out. The damage form is similar to the ridges and furrows of the ploughed land. (2) The splitting damage of the concrete is a form of brittle failure. It is a very dangerous pattern of bonding damage. Since the rebar is not sufficiently constrained laterally, the extrusion of the rebar against the concrete produces a radial force, which brings splitting cracks between the rebar and the concrete. Once the load reaches the limit, the block will give off a loud noise, and disintegrate into fragments.

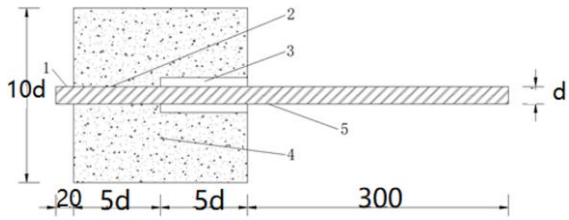


**Figure 1.** Central pull-out sample

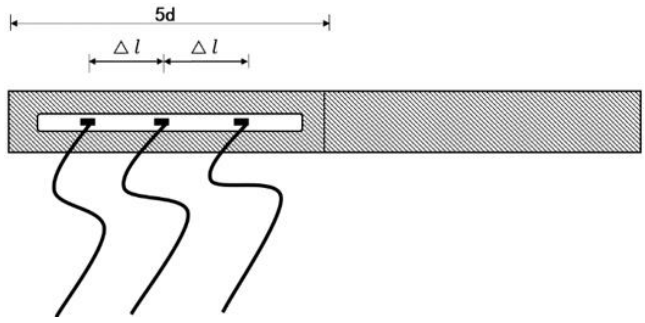


**Figure 2.** Slot opening and gage application

(1) Pull-out damage of rebar

(2) Splitting damage of concrete

**Figure 3.** Damage forms of specimens

**Table 1.** Compressive and splitting strengths of the concrete blocks

| Block number | Compressive strength /MPa (28d) | Compressive strength /MPa (90d) | Splitting strength/MPa (28d) | Splitting strength /MPa (90d) |
|---|---|---|---|---|
| $A_1$ | 44.2 | 53.2 | 3.05 | 3.67 |
| $A_2$ | 38.9 | 46.5 | 2.77 | 3.27 |
| $A_3$ | 40.2 | 48.3 | 2.89 | 3.36 |
| $A_4$ | 40.9 | 49 | 2.87 | 3.39 |
| $B_1$ | 47.5 | 59.4 | 3.42 | 4.08 |
| $B_2$ | 43.4 | 52.6 | 2.93 | 3.46 |
| $B_3$ | 44.3 | 53.8 | 3.15 | 3.78 |
| $B_4$ | 46.4 | 56.2 | 3.06 | 3.74 |

**Table 2.** Ultimate bonding stress, ultimate slip, and damage forms

| Block number | Ultimate load | Ultimate bonding stress | Ultimate slip | Relative difference of bonding stress | Pull-out damage | Splitting damage |
|---|---|---|---|---|---|---|
| C35-1-d18 | 130 | 25.56 | 2.05 | - | 0 | 3 |
| C35-2-d18 | 121 | 23.79 | 2.35 | -6.92% | 0 | 3 |
| C35-3-d18 | 128 | 25.16 | 2.16 | -1.56% | 1 | 2 |
| C35-4-d18 | 132 | 25.95 | 1.98 | +1.53% | 1 | 2 |
| C40-1-d18 | 136 | 26.74 | 1.88 | - | 1 | 2 |
| C40-2-d18 | 127 | 24.97 | 2.11 | -6.62% | 1 | 2 |
| C40-3-d18 | 130 | 25.56 | 2.04 | -4.41% | 0 | 3 |
| C40-4-d18 | 138 | 27.13 | 1.95 | +1.46% | 2 | 1 |
| C35-1-d25 | 228 | 23.24 | 2.36 | - | 0 | 3 |
| C35-2-d25 | 210 | 21.40 | 2.66 | -7.92% | 0 | 3 |
| C35-3-d25 | 214 | 21.81 | 2.51 | -6.15% | 0 | 3 |
| C35-4-d25 | 230 | 23.44 | 2.24 | +0.86% | 0 | 3 |
| C40-1-d25 | 236 | 24.05 | 2.13 | - | 0 | 3 |
| C40-2-d25 | 218 | 22.22 | 2.43 | -7.61% | 0 | 3 |
| C40-3-d25 | 231 | 23.54 | 2.35 | -2.12% | 0 | 3 |
| C40-4-d25 | 238 | 24.25 | 2.21 | +0.83% | 0 | 3 |

As shown in Table 2, with the growing grade of concrete strength, the bonding strength between rebar and concrete in the samples made from different materials all exhibited a continuous upward trend. For the samples of the same concrete strength, materials, and aggregate, the growth of rebar diameter would push up the ultimate load, and suppress the bonding strength. This is because a larger rebar diameter reduces the relative area, which weakens the bonding strength of reinforced concrete.

Figure 4 displays the mean bond slip curves between concrete and rebar. Since most central pull-out samples suffer from splitting damage, the declining segment of their bond slip curves was not obvious or simply absent. It can be inferred that, when the concrete grade and rebar diameter remain the same, the bond slip curves of concrete made from different materials had similar trends; the bonding stress difference between concrete made from different materials was not significant: Although there was no obvious law for the bond slip, most bond slip values concentrated in 1.88mm-2.66mm.

Figure 5 presents the bonding stress distribution curves. It can be observed that the bonding stress was zero at the free end and the load end, and peaked at 20-30mm from the load end. Along the anchor length, the bonding stress gradually decreased from the load end. At the same distance from the load end, the rebar-concrete bonding stress of the IOT concrete was slightly greater than that of the fly ash concrete. By the bonding stress, the different types of concrete can be ranked in descending order as IOT concrete, fly ash concrete, IOT powder concrete, and IOT power-IOT sand concrete.

Figure 6 compares the relative slip distribution curves of different samples. In the initial stage of loading, the relative slip first occurred at the load end, and appeared the latest on the free end. With the growth of the load, the stress propagated towards the free end, and the bonding effect between rebar and concrete was gradually damaged. Along the anchor length, the slip basically increased at a uniform rate. When the free end slipped, the slip rose prominently with the load. At the same distance from the load end, the relative slip of the fly ash

concrete was slightly higher than that of the IOT concrete, and much higher than that of the IOT power-IOT sand concrete. The IOT power concrete witnessed the greatest relative slip.

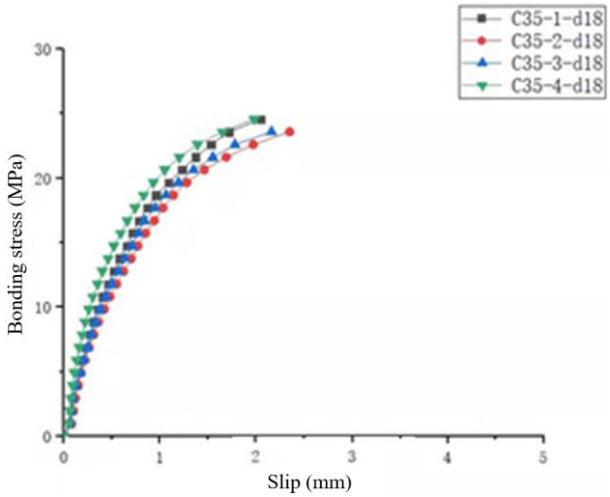


**Figure 4.** Mean bond slip curve of each type of concrete

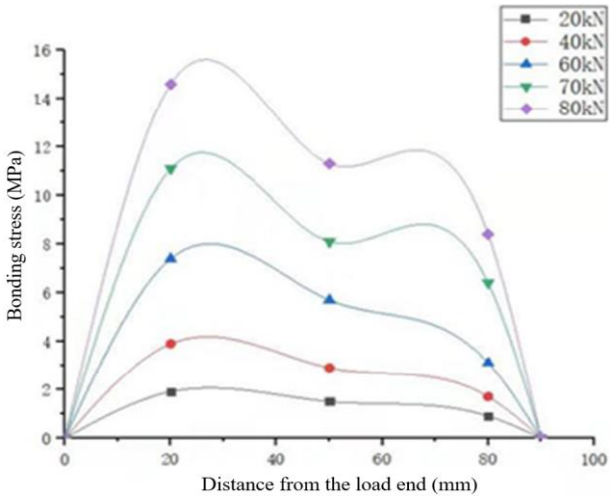


**Figure 5.** Bonding stress distribution curves of samples

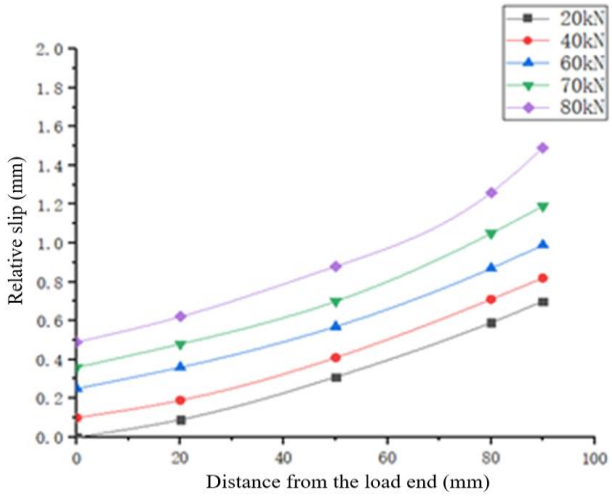


**Figure 6.** Change law of relative slip along the anchor length

Figure 7 shows the constitutive relationship between thermal stress and thermal strain of reinforced concrete under high temperatures. Figures 8 and 9 illustrate the temperature changes at measuring points in the cross-section of reinforced concrete columns, and the axial deformations of reinforced concrete columns, respectively, and compare the finite-element results with the test values. It can be seen that the temperature changes obtained by finite-element calculation basically agree with the test values at measuring points in the cross-section of each reinforced concrete column. The error between calculated and test values maximized at only 60°C, after the temperature increased continuously for 100min. Meanwhile, the axial deformations obtained by finite-element calculation had a large difference from the test values, but the axial deformation curves followed roughly the same trend as the temperature change curves. The gap between calculated and tested axial deformations peaked at 50-60min. The above analysis shows that the above simulation of the temperature field and mechanical performance of reinforced concretes fully demonstrate the thermal stress-thermal strain response mechanism.

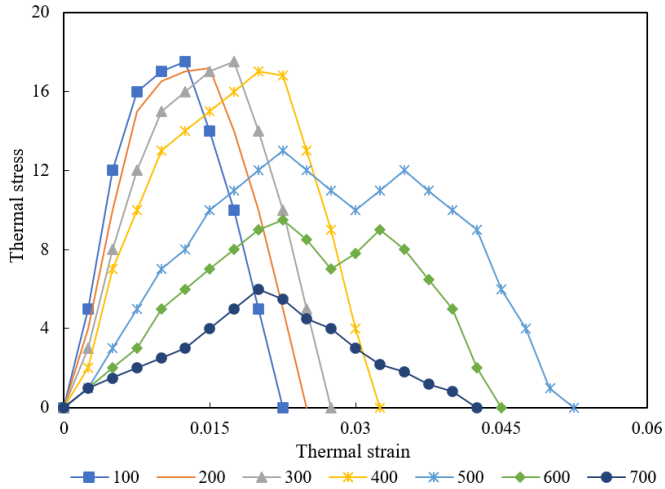


**Figure 7.** Relationship between thermal stress and thermal strain of concretes under high temperatures

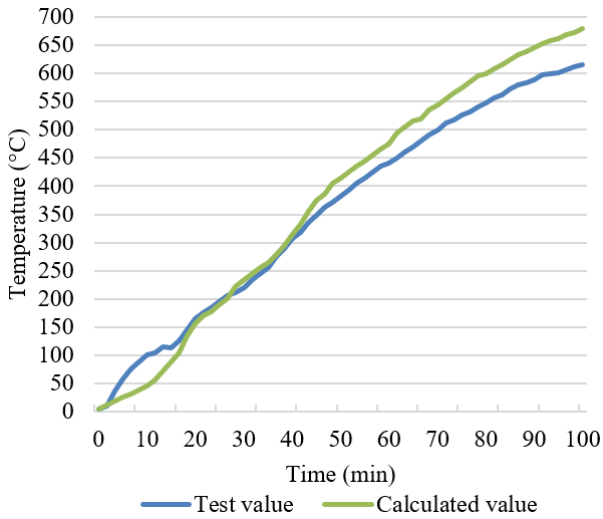


**Figure 8.** Temperature changes at measuring points in the cross-section of reinforced concrete columns

Figures 10 (1) and (2) report the temperature rise and axial deformation of reinforced concrete columns of the reduced scale of 1, 0.8, and 0.4, respectively. At the same time, the temperature rise curve of the column of the reduced scale of 1 was below that of any other column. In the first 5min of

heating, the temperature rise curves of all columns picked up quickly. As the heating lasted for 80min, the temperature rise curves of the columns varied significantly. When the heating reached 100min, the temperature difference was very small between the three temperature rise curves. Under high temperatures, the mechanical performance similarity between the columns of different reduced scales was correlated with their temperature field similarity. In the early phase of the axial expansion for reinforced concrete, the correlation was weak for the column with a relatively small reduced scale. In the late phase, the temperature field similarity between columns of different reduced scales continued to increase. As the heating time reached 100min, the difference in fire resistance rating between columns of different reduced scales dropped to the minimum.

Figures 10 (1) and (2) report the temperature rise and axial deformation of reinforced concrete columns of the reduced scale of 1, 0.8, and 0.4, respectively. At the same time, the temperature rise curve of the column of the reduced scale of 1 was below that of any other column. In the first 5min of heating, the temperature rise curves of all columns picked up quickly. As the heating lasted for 80min, the temperature rise curves of the columns varied significantly. When the heating reached 100min, the temperature difference was very small between the three temperature rise curves. Under high temperatures, the mechanical performance similarity between the columns of different reduced scales was correlated with their temperature field similarity. In the early phase of the axial expansion for reinforced concrete, the correlation was weak for the column with a relatively small reduced scale. In the late phase, the temperature field similarity between columns of different reduced scales continued to increase. As the heating time reached 100min, the difference in fire resistance rating between columns of different reduced scales dropped to the minimum.

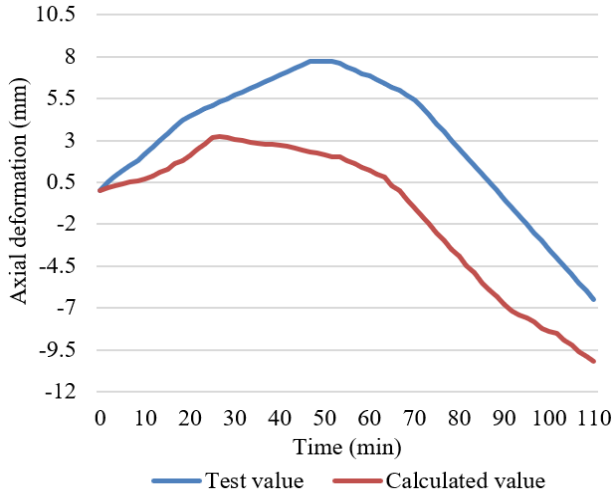


**Figure 9.** Axial deformations of reinforced concrete columns

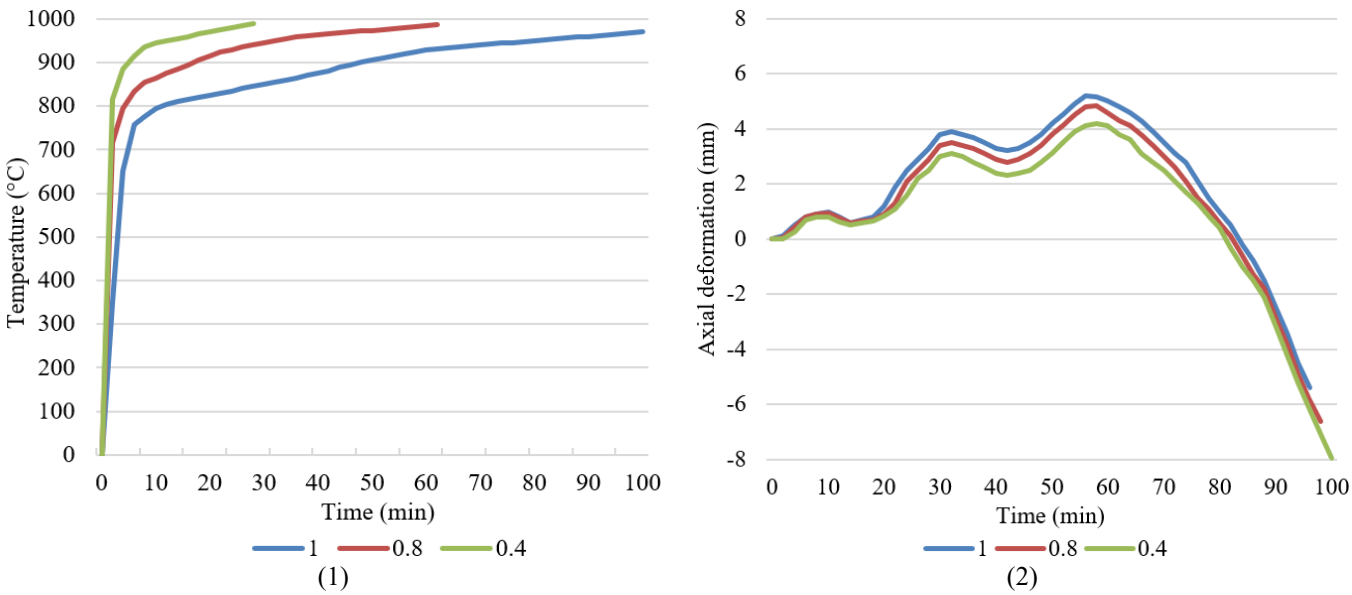


**Figure 10.** Temperature rise and axial deformation of reinforced concrete columns

## 5. CONCLUSIONS

This paper mainly investigates the bonding performance and thermomechanical coupling mechanism of IOT reinforced concrete. Firstly, the authors provided a bond slip curve model for the IOT-reinforced concrete interface, presented a strategy for drawing the mean bond slip curve, and computed the bond stress distribution, plus the local bond stress-relative slip distribution. Next, the thermal parameters of the IOT concrete material were summarized, and the high-temperature relationship between thermal stress and thermal strain was identified clearly. After that, central pull-out samples were prepared, and strain gages were applied to the slots of rebars. Through 16 sets of central pull-out tests, the authors summed up the results on the bonding performance and thermomechanical coupling analysis of IOT reinforced concrete. The main conclusions are as follows:

(1) In the initial stage of loading, the relative slip concentrated at the load end. With the growth of the load, the stress propagated towards the free end along the anchor length. When slip occurred at the free end, the slip rose prominently with the load, and gradually surpassed the ultimate bonding capacity, resulting in damages to the concrete. These phenomena are common among all types of concrete samples.

(2) According to the comparative analysis on the measured data, the bonding performance improves with the rising

strength grade of concrete, and weakens with the growth of rebar diameter.

(3) The mean bond slip curves and stress distribution curves of different types of IOT reinforced concrete were basically similar to those of fly ash concrete. Judging by the bonding stress distribution curve, the IOT concrete has a more uniform bonding stress, and greater bonding stress than fly ash concrete.

(4) The authors displayed the temperature changes at measuring points in the cross-section of reinforced concrete columns, and the axial deformations of reinforced concrete columns. The results show that our simulation of the temperature field and mechanical performance of reinforced concretes fully demonstrate the thermal stress-thermal strain response mechanism.

(5) The authors also reported the temperature rise and axial deformation of reinforced concrete columns of different reduced scales. The results show that, under high temperatures, the mechanical performance similarity between the columns of different reduced scales was correlated with their temperature field similarity. With the elapse of time, the difference in fire resistance rating between columns of different reduced scales dropped to the minimum.

## REFERENCES


[1] Kim, C.G., Park, H.G., Hong, G.H., Lee, H., Suh, J.I. (2018). Shear strength of reinforced concrete-composite beams with prestressed concrete and non-prestressed concrete. ACI Structural Journal, 115(4): 917-930. https://doi.org/10.14359/51702224

[2] Lu, Y., Henry, R.S. (2017). Numerical modelling of reinforced concrete walls with minimum vertical reinforcement. Engineering Structures, 143: 330-345. https://doi.org/10.1016/j.engstruct.2017.02.043

[3] Zhang, L., Sun, L. (2017). Effect of concrete carbonation on natural frequency of reinforced concrete beams. Advances in Structural Engineering, 20(3): 316-330. https://doi.org/10.1177%2F1369433216649728

[4] Gopinath, S., Murthy, A.R., Iyer, N.R., Prabha, M. (2015). Behaviour of reinforced concrete beams strengthened with basalt textile reinforced concrete. Journal of Industrial Textiles, 44(6): 924-933. https://doi.org/10.1177%2F1528083714521068

[5] Deng, Z.C., Zhang, W.C. (2015). Flexural performance of reinforced concrete beams reinforced with hybrid fiber reactive powder concrete. Harbin Gongcheng Daxue Xuebao/Journal of Harbin Engineering University, 36(9): 1199-1205.

[6] Lee, J.Y., Kim, K.H., Lee, S.H., Kim, C., Kim, M.H. (2018). Maximum torsional reinforcement of reinforced concrete beams subjected to pure torsion. ACI Structural Journal, 115(3): 749-760. https://doi.org/10.14359/51701108

[7] Zhu, C.J., Fang, S., Ng, P.L., Pundienė, I., Chen, J.J. (2020). Flexural behavior of reinforced concrete beams strengthened by textile reinforced magnesium potassium phosphate cement mortar. Frontiers in Materials, 7: 272. https://doi.org/10.3389/fmats.2020.00272

[8] Guérin, M., Mohamed, H.M., Benmokrane, B., Shield, C.K., Nanni, A. (2018). Effect of glass fiber-reinforced polymer reinforcement ratio on axial-flexural strength of reinforced concrete columns. ACI Structural Journal, 115(4): 1049-1061. https://doi.org/10.14359/51701279

[9] Zdanowicz, K., Kotynia, R., Marx, S. (2019). Prestressing concrete members with fibre- reinforced polymer reinforcement: State of research. Structural Concrete, 20(3): 872-885. https://doi.org/10.1002/suco.201800347

[10] Pucinotti, R. (2015). Reinforced concrete structure: Non destructive in situ strength assessment of concrete. Construction and Building Materials, 75: 331-341. https://doi.org/10.1016/j.conbuildmat.2014.11.023

[11] Kang, H., Ma, W., Zhang, K. (2015). Experimental investigation on specimen size effect of ferrous tailings concrete compressive strength. Metallurgical and Mining Industry, 2015(6): 289-294.

[12] Zhu, Z., Li, B., Zhou, M. (2015). The influences of iron ore tailings as fine aggregate on the strength of ultra-high performance concrete. Advances in Materials Science and Engineering, 2015: 412878. https://doi.org/10.1155/2015/412878

[13] Wang, X., Yu, R., Shui, Z., Zhao, Z., Song, Q., Yang, B., Fan, D. (2018). Development of a novel cleaner construction product: Ultra-high performance concrete incorporating lead-zinc tailings. Journal of Cleaner Production, 196: 172-182. https://doi.org/10.1016/j.jclepro.2018.06.058

[14] Kathirvel, P., Kwon, S.J., Lee, H.S., Karthick, S., Saraswathy, V. (2018). Graphite ore tailings as partial replacement of sand in concrete. ACI Materials Journal, 115(3): 481-492.

[15] Gou, M., Zhou, L., Then, N.W.Y. (2019). Utilization of tailings in cement and concrete: A review. Science and Engineering of Composite Materials, 26(1): 449-464. https://doi.org/10.1515/secm-2019-0029

[16] Liang, X., Wang, C., Zhan, J., Cui, X., Ren, Z. (2019). Study on preparation of eco-friendly autoclaved aerated concrete from low silicon and high iron ore tailings. Journal of New Materials for Electrochemical Systems, 22(4): 224-230. https://doi.org/10.14447/jnmes.v22i4.a08

[17] Zhao, J., Su, Y., Shi, Y., Wang, Q., Ni, K. (2022). Study on mechanical properties of macro- synthetic fiber-reinforced iron ore tailings concrete. Structural Concrete, 23(1): 423-440. https://doi.org/10.1002/suco.202100383

[18] Gu, X., Li, X., Zhang, W., Gao, Y., Kong, Y., Liu, J., & Zhang, X. (2021). Effects of HPMC on workability and mechanical properties of concrete using iron tailings as aggregates. Materials, 14(21): 6451. https://doi.org/10.3390/ma14216451

[19] Ashkezari, G.D., Razmara, M. (2020). Thermal and mechanical evaluation of ultra-high performance fiber-reinforced concrete and conventional concrete subjected to high temperatures. Journal of Building Engineering, 32: 101621. https://doi.org/10.1016/j.jobe.2020.101621

[20] Makeeva, A., Amelina, A., Semenov, K., Barabanshchikov, Y. (2018). Temperature action in analysis of thermal stressed state of massive concrete and reinforced concrete structures. MATEC Web of Conferences, 245: 03016. https://doi.org/10.1051/matecconf/201824503016